J. Fluid Mech. (2002), *vol.* 465, *pp.* 213–235.
DOI: 10.1017/S0022112002001155 Printed in the United Kingdom

Oscillatory forcing of flow through porous media. Part 1. Steady flow

By D. R. GRAHAM AND J. J. L. HIGDON

Department of Chemical Engineering, University of Illinois, Urbana, IL 61801, USA

(Received 5 November 1998 and in revised form 27 December 2001)

Oscillatory forcing of a porous medium may have a dramatic effect on the mean flow rate produced by a steady applied pressure gradient. The oscillatory forcing may excite nonlinear inertial effects leading to either enhancement or retardation of the mean flow. Here, in Part 1, we consider the effects of non-zero inertial forces on steady flows in porous media, and investigate the changes in the flow character arising from changes in both the strength of the inertial terms and the geometry of the medium. The steady-state Navier–Stokes equations are solved via a Galerkin finite element method to determine the velocity fields for simple two-dimensional models of porous media. Two geometric models are considered based on constricted channels and periodic arrays of circular cylinders. For both geometries, we observe solution multiplicity yielding both symmetric and asymmetric flow patterns. For the cylinder arrays, we demonstrate that inertial effects lead to anisotropy in the effective permeability, with the direction of minimum resistance dependent on the solid volume fraction. We identify nonlinear flow phenomena which might be exploited by oscillatory forcing to yield a net increase in the mean flow rate. In Part 2, we take up the subject of unsteady flows governed by the full time-dependent Navier–Stokes equations.

1. Introduction

The transport of viscous fluids through porous media is a problem of wide ranging interest in engineering applications. Flow through porous media is encountered in environmental problems involving groundwater transport, oil recovery processes in the petroleum industry, flow through packed beds and filtration processes arising in manufacturing processes. Over the years, a large body of research has been devoted to this subject with the primary emphasis on the steady low Reynolds number flows commonly encountered in applications. Recently, we have become interested in flows at finite Reynolds number for which inertial effects may play an important role both in steady and unsteady flows. For certain porous media, such as packed beds and heat exchanger tube bundles, the pore length scales are such that finite Reynolds number flows may be encountered as part of normal steady-state operations. The scope of our present study includes these cases, but the primary focus will be on the effect of inertial forces introduced by unsteady oscillatory forcing. We shall see that such forcing may induce strong inertial flows and interesting transport phenomena in media with pore length scales as small as 20 microns.

One of the distinct features of oscillatory forcing is that it is possible to reach significant pore-scale Reynolds numbers in porous media where such Reynolds numbers would be impossible to achieve in a steady pressure-driven flow. The oscillatory forcing may be introduced through a number of mechanisms a few examples of which are

cited below. For porous media encountered in a manufacturing setting, the oscillatory force may be introduced by placing the porous flow device on an oscillating platform driven by a mechanical oscillation. For larger scale devices, the basic medium may remain fixed and the oscillatory motion induced by a pressure wave travelling through the solid matrix. Such waves may be excited by mechanically driven oscillators or through ultrasonic transducers. In each of these cases, the local effect on the pore scale is to induce an acceleration of the solid matrix. In a non-inertial reference frame which moves with the solid, the effect of the solid acceleration is exactly equivalent to an oscillatory body force acting on the fluid. The important point is that each pore of the porous medium experiences the same body force per unit volume, which is given by the product of the fluid density and the local acceleration of the medium. In steady pressure-driven flow, the pressure drop across each pore is equal to the total pressure drop divided by the number of pores in the direction of flow. Since the number of pores spanning the medium may range from hundreds to tens of thousands, a significant Δp across a single pore would require a total pressure head 10^2 to 10^4 times higher. It is this multiplier which makes it difficult to achieve moderate Reynolds numbers in steady flow, while they are easily accessible in oscillatory flow.

One of the more intriguing applications for oscillatory forcing in porous media arises in the field of enhanced oil recovery. In a large fixed petroleum reservoir, mechanical translation is impossible and one relies on the alternative strategy involving an acoustic wave travelling through the solid matrix. Acoustic wave propagation through petroleum reservoirs has been employed as an exploration tool for decades, but it is only in recent years that it has been considered as a mechanism to stimulate oil production. Laboratory and field tests (Beresnev & Johnson 1994) have shown that acoustic stimulation can increase the effective permeability of the porous medium resulting in higher flow rates for a given pressure drop. In addition, the stimulation may increase the mobility of the oil phase relative to the water phase yielding a higher concentration of oil in the product stream. The feasibility of acoustic stimulation in petroleum reservoirs depends on the development of robust transducers which can be placed downhole in oil wells to deliver strong local acoustic fields. This is an active area of research and development among equipment manufacturers (Drake & Beresnev 1999), and novel designs show significant promise.

While the exact physical mechanisms for enhanced oil production through acoustic stimulation are unclear, there are a number of possible explanations based on the fluid dynamics of both multiphase and single-phase flow. In multiphase flow, acoustic oscillations may act to force a suspended oil droplet through a narrow constriction, to reduce the flow resistance by deforming the droplet or to displace droplets attached to solid surfaces. These multiphase mechanisms have been the subject of previous studies in our research group (Dimitrakopoulos & Higdon 1997, 1998; Graham & Higdon 2000*a*, *b*). In the present effort, we investigate possible mechanisms involving single-phase flow. In particular, we consider how the general phenomenon of oscillatory forcing in porous media may affect the flow resistance or mean flow rate in pressure-driven flows through porous media.

The goal of the present effort is to conduct a computational study on the effect of oscillatory forcing on flow through porous media. Here, in Part 1, we analyse steady flow through simple geometric models of porous media and determine the impact of inertial effects on the flow rate produced by a given pressure gradient. In Part 2 (Graham & Higdon 2002), we consider the effect of acoustic stimulation and show how the nonlinear interaction of mean and fluctuating pressure forces affects the average flow rate. In this investigation, we shall show that single-phase flow

mechanisms provide one path to enhanced transport via oscillatory forcing in porous media.

The simple geometric models utilized in this study are two-dimensional periodic media consisting of constricted channels and cylinder arrays. Previous work on flow in constricted channels and capillary tubes has characterized the effect of geometrical features on the flow behaviour in several regimes. Stokes flow in two-dimensional sinusoidal channels was studied by Pozrikidis (1987) who determined the permeability and flow patterns in these models. Similar results were presented by Hemmat & Borhan (1995) for constricted capillary tubes. Both studies showed that separated flow with regions of reversed flow can occur within a certain range of parameters. The effects of finite Reynolds number have been studied by Deiber & Schowalter (1979) and Ralph (1987). These authors observed regions of flow reversal and found a nonlinear relationship between the flow rate and pressure gradient. Ralph showed that the mean pressure gradient increases as the perturbation amplitude and wavelength decrease for tubes in which the minimum constriction radius is held constant.

Our second geometric model is a doubly periodic square array of circular cylinders. This geometry has been studied by a large number of authors. Early results for Stokes flow in dilute arrays were presented by Hasimoto (1959), while more extensive results were given by Sangani & Acrivos (1982) and Larson & Higdon (1987). Larson & Higdon presented microscopic streamline patterns showing small regions of recirculation close to the cylinders. Finite Reynolds number flow through periodic arrays of cylinders was studied by Edwards *et al.* (1990). These authors found that inertial effects decreased the effective permeability and produced an anisotropic permeability tensor. In a more recent study, Koch & Ladd (1997) analysed the anisotropy for square arrays of cylinders. For solid volume fractions less than 40%, they showed that the permeability for flow aligned with the lattice vectors was greater than that for flow at other angles.

To characterize the flow behaviour at finite Reynolds number completely, one must consider the possibility of multiple solutions. Previous studies have shown the existence of multiple solutions for geometries similar to the constricted channels discussed in this work. In an early effort Fraenkel (1962, 1963) employed perturbation expansions to study the bifurcation structures in converging and diverging channels with small wall angles. Later studies have employed numerical computations and experiments to investigate sharper expansions and contractions. For flow through a sudden expansion, Fearn, Mullin & Cliffe (1990) found a single, symmetric solution at low Reynolds number, but showed a symmetry-breaking bifurcation at higher Reynolds number yielding two mirror-image asymmetric flows. Goodwin & Schowalter (1996) studied the case of two jets flowing into a symmetric channel and reported a complicated pattern of solutions with a high degree of multiplicity. Sobey & Drazin (1986) report multiple asymmetric solutions for a channel with an expansion throat upstream followed by a contraction downstream with plane walls in between. Based on this evidence, we infer that solution multiplicity is a common occurrence in confined flows at finite Reynolds number. We shall see that this phenomenon is indeed prevalent in the results of the present investigation.

The main thrust of our study is to determine the mechanisms by which oscillatory forcing may be exploited for enhanced transport in flow through porous media. The direct investigation of these phenomena is conducted in Part 2. In Part 1, our goal is conduct prerequisite studies to characterize the steady flow behaviour in the geometric models for the porous media. Later, we shall see that knowledge of the steady flow behaviour provides the key to understanding many of the

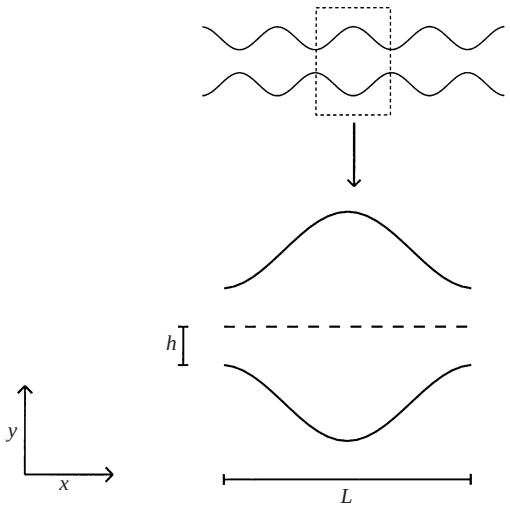

FIGURE 1. Schematic of a constricted channel.

oscillatory flow phenomena. In our investigation of the steady flows, we encounter many phenomena which have been previously observed by researchers cited above. These phenomena include: symmetric flow patterns at low Reynolds number, fore–aft asymmetry and flow separation at moderate *Re*, and flow bifurcations and multiple solutions at higher Reynolds numbers. Given that such phenomena have been well characterized in other systems, we shall forego a detailed study of the flow morphology and focus our attention on the means through which these phenomena affect the oscillatory forcing mechanisms. In addition to the characterization of the flow fields, we shall focus our efforts on the quantitative computation of the flow resistance in our model geometries. These quantitative data will prove essential in developing predictions for the oscillatory flow phenomena encountered in Part 2.

2. Problem description and numerical methods

2.1. *Geometric models*

We begin by defining the two geometric models of porous media used in this study. The constricted channel model is shown schematically in figure 1, with the positions of the top and bottom walls given by

$$y = \pm\left\{h + a\left[1 + \sin\left(\frac{2\pi x}{L}\right)\right]\right\}, \tag{2.1}$$

where h is the half-width of the channel, L is the wavelength and a is the amplitude. The two geometric parameters that characterize this model are the dimensionless constriction size h/a and dimensionless wall slope ak, where $k = 2\pi/L$.

For the second geometrical model, we consider a two-dimensional array of cylinders, shown in figure 2. The single geometric parameter for this model is the gap size, h, non-dimensionalized with the cylinder radius as h/r. Note that the geometry could also be parameterized by the solid volume fraction; however, the gap size h/r provides a more natural measure for comparison with the constricted channels.

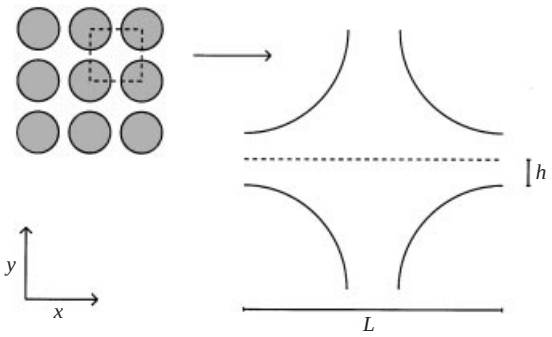

FIGURE 2. Schematic of an array of cylinders.

2.2. *Governing equations*

The governing equations for the steady flow of an incompressible Newtonian fluid are the Navier–Stokes equations and the continuity equation,

$$\rho \boldsymbol{u} \cdot \nabla \boldsymbol{u} = -\nabla P + \mu \nabla^2 \boldsymbol{u} + \boldsymbol{b}, \tag{2.2}$$

$$\nabla \cdot \boldsymbol{u} = 0. \tag{2.3}$$

The no-slip boundary condition is imposed on the solid boundaries

$$\boldsymbol{u} = \boldsymbol{0} \qquad \text{on} \qquad S_b, \tag{2.4}$$

where S_b represents either the walls of the constricted channel or the surface of the cylinders. Periodic boundary conditions,

$$\boldsymbol{u}(\boldsymbol{x}) = \boldsymbol{u}(\boldsymbol{x} + \boldsymbol{L}) \tag{2.5}$$

are applied at the inlet and outlet. The pressure P at the inlet and outlet differs by a fixed constant owing to the applied pressure gradient $\boldsymbol{G}$,

$$P(\boldsymbol{x}) = P(\boldsymbol{x} + \boldsymbol{L}) + \boldsymbol{G} \cdot \boldsymbol{L}. \tag{2.6}$$

To implement the boundary conditions, it proves convenient to work with a periodic function for the pressure. To accomplish this goal, we add a body force term equal to the applied pressure gradient

$$\boldsymbol{b} = \boldsymbol{G} \tag{2.7}$$

to the Navier–Stokes equations so that the pressure at the inlet is equal to the pressure at the outlet.

The primary goal of our study is to solve the boundary value problem for the velocity field and to determine the effect of the applied pressure gradient on the overall flow rate. To characterize the flow rate, we define the average velocity U as

$$U = \frac{1}{2h} \int_{-h}^{h} \boldsymbol{u} \cdot \boldsymbol{n} \, \mathrm{d}S. \tag{2.8}$$

We non-dimensionalize all quantities relative to the set of parameters h, ρ and v, where ρ and v are the fluid density and kinematic viscosity respectively. With this choice, the dimensionless flow rate is the Reynolds number

$$Re_o = Uh/v \tag{2.9}$$

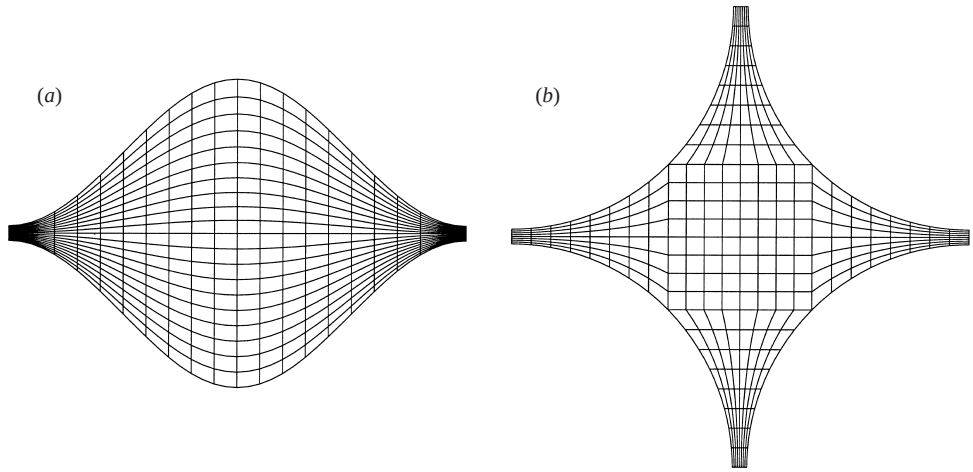

FIGURE 3. Finite element mesh for (*a*) a constricted channel and (*b*) an array of cylinders.

and the dimensionless pressure gradient is defined as

$$\boldsymbol{F}_o = \boldsymbol{G}h^3/\rho\nu^2. \tag{2.10}$$

For the cylinder arrays, we find it convenient to break $\boldsymbol{F}_o$ into its x- and y-components, F_{xo} and F_{yo}, while for the constricted channel, there is a single component F_{xo}. For the steady-state calculations, we are interested in the net flow rate as a function of the applied pressure gradient and the geometrical parameters. In dimensionless terms, we compute the Reynolds number as a function of ak, h/a and $\boldsymbol{F}_o$.

2.3. *Numerical methods*

The nonlinear elliptic boundary value problem defined by equations (2.2) to (2.6) was solved using the Galerkin finite element method. Velocities were interpolated using nine-node quadratic elements and pressures were interpolated with three linear basis functions. This formulation satisfies conservation of mass on an elemental basis and avoids over-constraint problems (Huyakorn *et al.* 1978). Transfinite interpolation was utilized (Thompson, Warsi & Mastin 1985) to generate the algebraically mapped grids needed for the Galerkin finite element method. A sample mesh for the constricted channel is shown in figure 3(*a*), and a mesh for the cylinder array model is presented in figure 3(*b*).

Application of the Galerkin finite element method leads to a nonlinear system of algebraic equations

$$R_i(x_j) = 0, \tag{2.11}$$

where R_i is a vector of residuals corresponding to the momentum and continuity equations and x_j is a vector of unknowns corresponding to the nodal values of velocity and pressure. This system is solved iteratively with Newton's method

$$\left(\frac{\partial R_i}{\partial x_j}\right)^k \Delta x_j^{k+1} = -R_i{}^k, \tag{2.12}$$

where the superscript k is the iteration number, Δx_j is the change in nodal values and $\partial R_i/\partial x_j$ is the analytically evaluated Jacobian matrix. This system of equations was solved with SuperLU, a code that implements a sparse Gaussian elimination algorithm (Demmel *et al.* 1995). The initial velocity fields required for rapid convergence

Mesh	Re_o	Error
8×8	28.7620	6.4×10^{-2}
12×12	27.6327	2.2×10^{-2}
15×15	27.2606	8.3×10^{-3}
20×20	27.0831	1.7×10^{-3}
30×30	27.0416	1.8×10^{-4}
36×36	27.0380	4.4×10^{-5}

TABLE 1. Convergence test for $F_{xo} = 10$. The relative error was calculated using the result for a 40×40 mesh ($Re_o = 27.0368$).

Channel		Arrays	
Mesh	Re_o	Mesh	Re_o
16×16	61.58	$6 \times 6 \times 5$	52.96
20×20	61.33	$8 \times 8 \times 5$	53.21
24×24	61.34	$10 \times 10 \times 5$	53.26

TABLE 2. Convergence test for $F_{xo} = 35$ for a constricted channel and cylinder arrays.

of equation (2.12) were obtained by employing continuation in either body force, geometric parameters, or arc-length (Keller 1977).

While a continuation procedure can be employed effectively to map a given solution branch, it does not yield any information about the stability of the solutions. One way to determine the stability of a given solution is to linearize the governing equations and formulate an eigenvalue problem (Goodwin & Schowalter 1996). A major drawback to this technique is that the resulting eigenvalue problem is complex, which greatly increases the computational burden. We have found that an effective alternative to this procedure is to integrate the transient governing equations in time and directly observe the stability of a given solution. Further details of our algorithm for the unsteady flows are given in Part 2.

2.4. *Numerical tests*

Before proceeding with the main body of our results, we briefly document the accuracy of the numerical computations. Table 1 shows convergence data for the total flow rate Re_o as a function of the number of finite elements for flow through a constricted channel with wall slope $ak = 1$. These results show excellent convergence with a relative error reaching 4.4×10^{-5} for a 36×36 grid. For the bulk of the computations presented in this paper, the 20×20 grid was employed yielding a relative error of 1.7×10^{-3} in the flow rate. In certain cases, finer meshes were employed to confirm the validity of the results. Additional tests were conducted for a higher forcing level to confirm the same level of accuracy at higher Reynolds numbers. Table 2 gives convergence results for $F_{xo} = 35$ for constricted channels and for cylinder arrays. In each case, the total flow rate Re_{xo} has converged to a relative error of order 10^{-3}. Additional tests of the finite element algorithm were conducted to confirm the accuracy for unsteady flows as noted in Part 2.

3. Results

The primary goal here in Part 1 is to characterize the effect of inertial forces on fluid flow in constricted geometries which are representative of porous media. In the sections below, we present series of numerical computations which illustrate the basic features of these flows, and we document the dependence of the flow rate on the applied driving force. Our first series of computations focuses on the effects of increasing the driving force F_{xo} (and as a consequence the Reynolds number Re_o) in a constricted channel of fixed geometry. Next, we examine how changes in the geometry of the channel affect the flow behaviour in the presence of inertial forces. Upon completion of the studies for the constricted channel, we turn our attention to the periodic cylinder arrays. In considering this second geometry, we have two goals. The first is to verify that the results for the constricted channels have general applicability and relevance for other geometries, while the second is to investigate the effects of applied pressure gradients at different orientations relative to the geometry of the medium.

3.1. *Constricted channel*

We begin our investigation with flow in a constricted channel with wall slope $ak = 1$ and constriction size $h/a = 0.1$. The streamline patterns shown in figure 4 demonstrate the basic flow features in this system. At the lowest Reynolds numbers (figure 4*a*) streamline patterns exhibit symmetry with respect to both the x- and y-axes. As the flow rate increases (figure 4*b*), inertial effects become important and flows show fore–aft asymmetry with separated flow regions along the walls. At higher flow rates (figure 4*c*, *d*) bifurcations develop leading to multiple solutions at a given forcing level F_{xo} or flow rate Re_o. As the flow rate is increased further, the solution space exhibits an increasing degree of multiplicity. Figure 5 shows the streamline patterns for four solutions arising at a forcing level $F_{xo} = 35$. Multiple solutions in these systems include at least one y-symmetric solution and an even number of mirror image y-asymmetric solutions. Including the mirror images of figure 5(*b–d*), there are a total of seven solutions for the forcing level $F_{xo} = 35$.

The richness of the solution space which arises for the Navier–Stokes equations in channel flows with axially varying geometry has been well established in previous research efforts. In particular, Sobey & Drazin (1986) considered a rectangular channel with sudden expansion/contraction, while Goodwin & Schowalter (1996) studied a single expansion with two inlet jets. These authors presented bifurcation diagrams and detailed analysis documenting the wide range of turning points and bifurcations arising in these flows. The sinusoidal channels of the present study exhibit many of the same phenomena; however, the details of the solution space are significantly different owing to the change in the channel geometry. Given the specific goals of the present study, we shall not attempt to duplicate the detailed bifurcation analysis of prior efforts cited above. Instead, we focus on those details of the steady flows which will have significant impact on the oscillatory forcing mechanisms studied in Part 2.

The most important information which we require for oscillatory forcing is the quantitative data for the bulk flow rate Re_o as a function of forcing level (pressure gradient) F_{xo}. This is presented in figure 6(*a*) for the channel geometry $ak = 1$, $a/h = 0.1$ which we have considered above. For low Reynolds number flows, the flow rate is directly proportional to the pressure gradient, and the limiting slope as $Re_o \to 0$ gives the Darcy permeability for the channel. The curvature of the flow curves for higher Reynolds number indicates the increased resistance characteristic of inertial flows. In this figure, we observe that all solution branches yield approximately

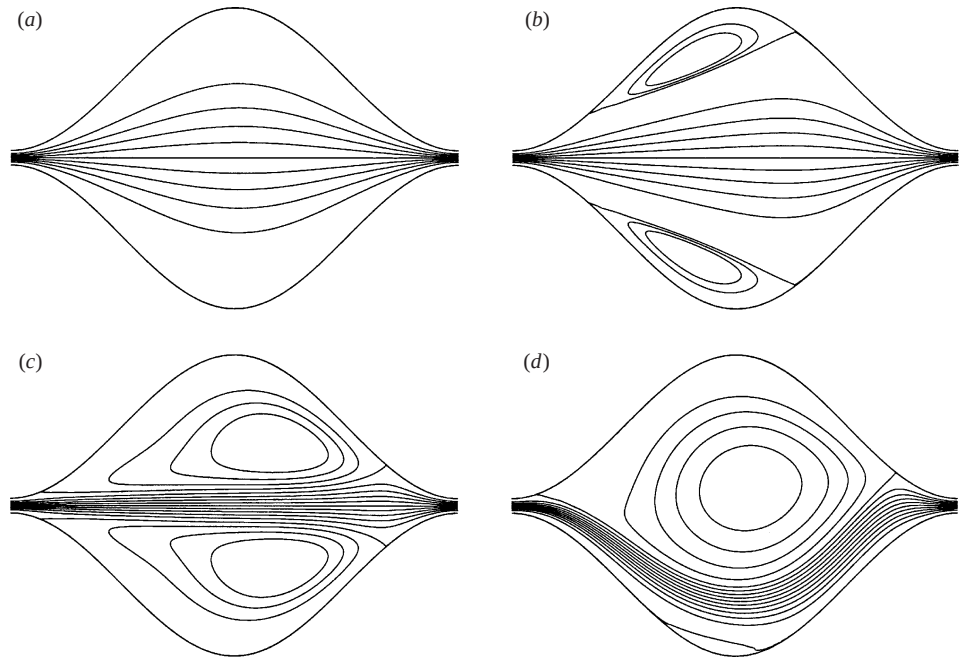

FIGURE 4. Streamline patterns for a channel ($ak = 1$, $h/a = 0.1$) showing change in flow pattern with increasing forcing level. (*a*) $F_{xo} = 0.25$, $Re_o = 0.925$; (*b*) $F_{xo} = 2$, $Re_o = 7.23$; (*c*) Symmetric flow, $F_{xo} = 10$, $Re_o = 27.1$; (*d*) Asymmetric flow, $F_{xo} = 10$, $Re_o = 26.6$.

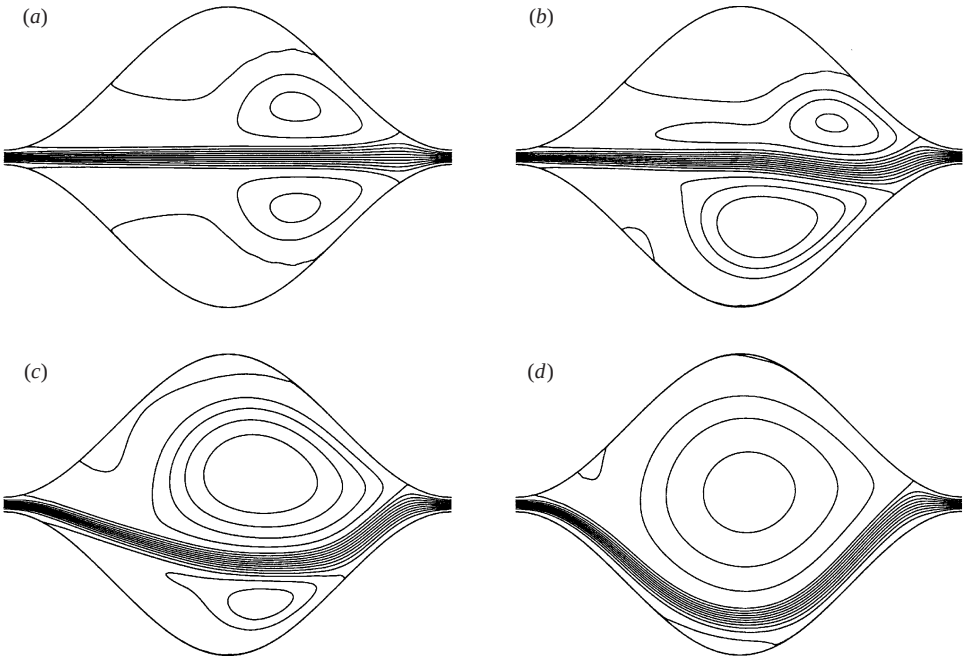

FIGURE 5. Streamline patterns for the four solutions present at forcing level $F_{xo} = 35$: (*a*) $Re_o = 63.9$, (*b*) $Re_o = 63.7$, (*c*) $Re_o = 62.8$, (*d*) $Re_o = 61.3$.

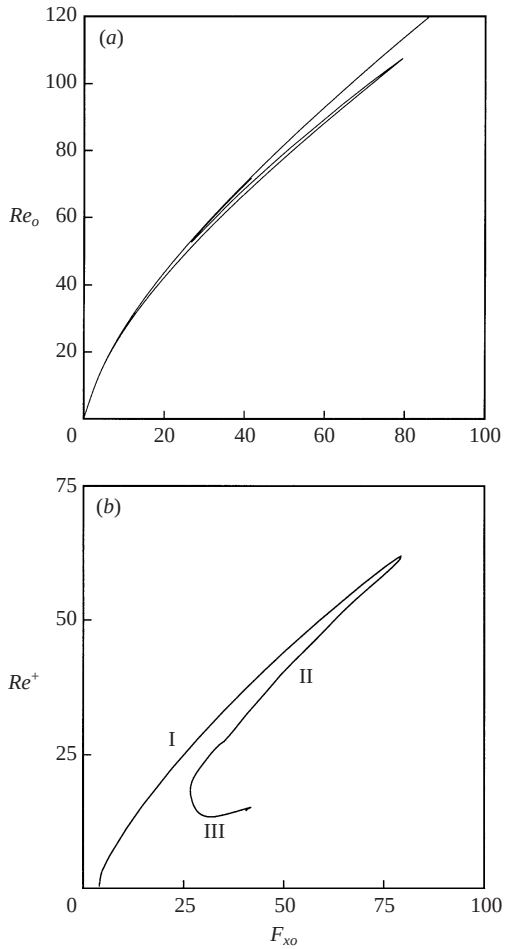

FIGURE 6. (*a*) Bulk flow rate Re_o as a function of forcing level F_{xo} for a constricted channel with $ak = 1$ and $h/a = 0.1$. (*b*) Bifurcation diagram illustrating the four solution branches; numerals identify different solution branches.

the same flow rate at a given forcing level. As a specific example, the streamline patterns shown in figure 5 for forcing level $F_{xo} = 35$ yield flow rates ranging from $Re_o = 61.3$ to $Re_o = 63.9$. While the net flow rate is comparable in each case, we shall later see that the symmetric/asymmetric character of the flow field plays a significant role in the presence of oscillatory forcing.

When multiple solutions exist in a given channel geometry, stability considerations dictate which solutions are most likely to be observed experimentally. We have determined the stability of each solution branch by considering small perturbations of the steady flow solution and computing the time-dependent solution through integration of the unsteady Navier–Stokes equations. Growth rates and frequencies of the least stable eigenmode were computed to an accuracy of 1–2% and verified by grid refinement. In cataloguing the stability of the different solution branches, a bifurcation diagram such as shown in figure 6(*a*) above often provides a useful reference frame. Unfortunately, in this figure the multiple solution branches fall so close together that it is difficult to discern the individual curves. To accentuate the

differences between different asymmetric flow branches, we define a control parameter similar to that employed by Sobey & Drazin and by Goodwin & Schowalter. In particular, we define a dimensionless measure Re^+ which reflects the asymmetry of the solutions:

$$Re^+ = \left[\frac{\int_A (u_x(x,y) - u_x(x,-y))^2 + (u_y(x,y) + u_y(x,-y))^2 \, \mathrm{d}A}{\int_A \mathrm{d}A} \right]^{1/2}. \qquad (3.1)$$

The bifurcation diagram figure 6(b) shows Re^+ as a function of F_{xo} for the same range of forcing level as for the flow rate plotted in figure 6(a). In this figure, a symmetric solution corresponds to the horizontal axis $Re^+ \equiv 0$. For low Reynolds numbers, a single symmetric stable solution exists up to a forcing level of approximately $F_{xo} = 4$. At this point, a bifurcation is reached and the symmetric branch loses stability to the asymmetric branch I seen in figure 6(b). The streamlines for solutions along this stable branch are represented by figures 4(d) and 5(d). This solution branch remains stable until it reaches the turning point near $F_{xo} = 80$. Continuing past the turning point, the solution branch II assumes the form of the streamline pattern 5(c) and it is unstable. The next turning point is reached at a forcing level $F_{xo} = 26$ after which the solution III takes the form illustrated in 5(b), and it is also unstable. We have followed the solution branch III 5(b) to higher forcing levels and find a number of additional turning points near $F_{x0} = 42$. While it was not possible to trace these solutions further, we note that additional solutions might exist beyond those which are shown in figure 6.

In many systems, the turning points on the bifurcation diagram mark transitions between stable and unstable solution branches, as for example with branches 5(c, d) here. It is possible however to encounter distinct unstable solution branches meeting at a turning point as in the case of branches 5(b, c). In general, the bifurcation diagram provides a useful guide to the solution space, but it is not possible to infer the solution stability directly from this figure. Further discussion of the stability behaviour in the presence of turning points is given by Sobey & Drazin who show examples of stable–unstable transitions (1986, figure 9), and by Goodwin & Schowalter (§ 3.3) who show turning points joining unstable branches.

We find it useful here to summarize our results for steady flows in constricted channels with $ak = 1$ and $h/a = 0.1$. At low forcing levels a single stable symmetric solution branch exists. Over a range of forcing from $F_{xo} = 4$ to $F_{xo} = 80$, multiple solutions exist; however it appears that there is a single stable solution with asymmetric form shown by figure 5(d) (or its mirror image). The bulk flow rate is a strong nonlinear function of the forcing level, but changes in the flow rate among different solutions at a given forcing level are small. Streamline patterns associated with the symmetric and asymmetric stable solutions show marked differences which may have consequences for oscillatory forcing as described later in Part 2.

Having characterized the $ak = 1$, $h/a = 0.1$ geometry, we turn our attention to channels with different gap sizes and wall slopes. Recall that we employ the constricted channels as models of porous media which often display a constriction–pore structure with large open pores interconnected by small irregular constrictions. To assess the sensitivity of the results to the model geometry, we vary the gap size (h/a) to model the effect of constriction size in real media, and we vary the wall slope (ak) as an indicator of the effect of pore size and geometry. We are most interested in the effects

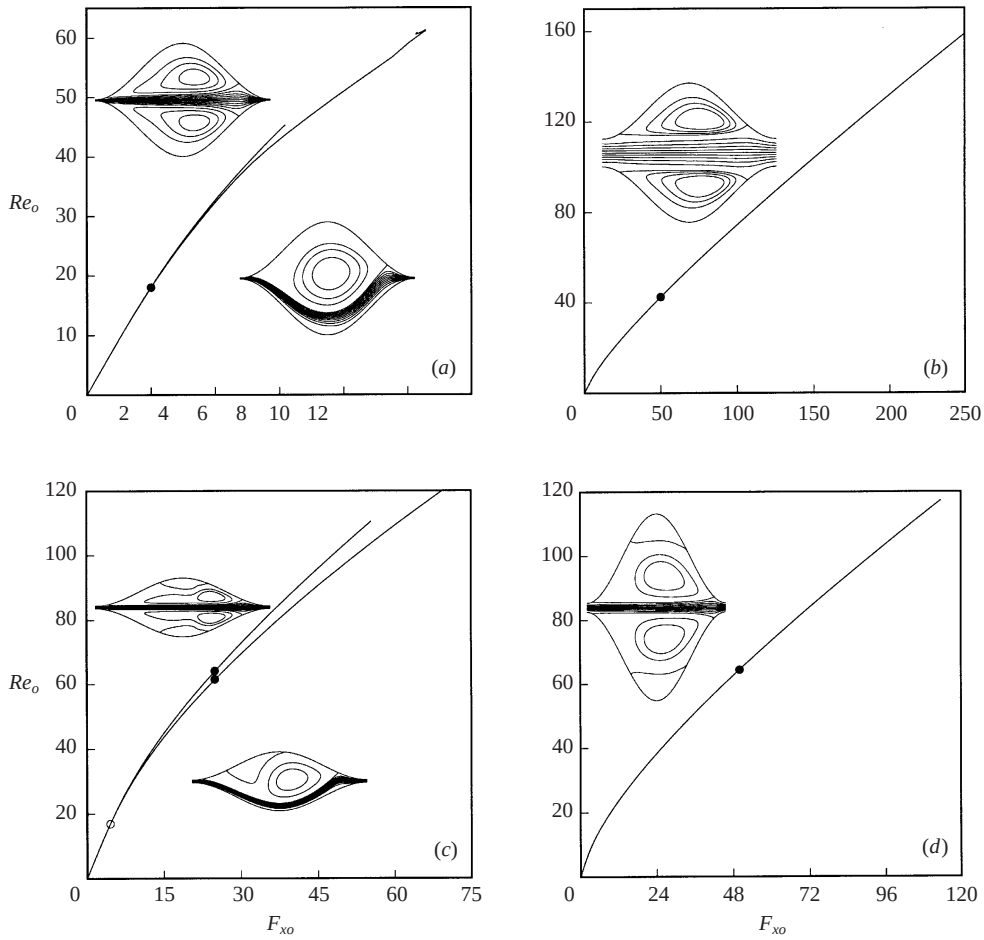

FIGURE 7. Bulk flow rate for a constricted channel with different geometrical parameters: (*a*) $ak = 1$, $h/a = 0.02$; (*b*) $ak = 1$, $h/a = 0.5$; (*c*) $ak = 0.5$, $h/a = 0.1$; (*d*) $ak = 2.0$, $h/a = 0.1$. Open circles indicate the location of bifurcation points and solid circles indicate the conditions for the inset streamline patterns.

of the geometry on the nonlinearity in the flow rate/forcing level curves and on the transition from symmetric to asymmetric flow patterns.

We begin with the effect of varying the gap size while keeping the wall slope constant at $ak = 1$. Figure 7(a, b) shows the flow rate for two channels with gap size $a/h = 0.02$ and $a/h = 0.50$ respectively; the insets show samples of the streamline patterns in each channel. Compared to the previous case $a/h = 0.1$, the channel with the smallest constriction (figure 7*a*) shows the emergence of an asymmetric flow pattern at a significantly lower forcing level $F_{xo} = 1$ compared to $F_{xo} = 4$ in the earlier case. By contrast, the channel with the widest gap shows no bifurcations and only a single symmetric solution over the entire range of forcing. For the smallest gap, the jet of fluid flowing along the channel axis in the symmetric solution is quite narrow, and it experiences a significant deceleration as it moves through the wide central part of the channel. The strong adverse pressure gradient associated with this deceleration decreases the stability of the jet and leads to the transition to the asymmetric flow pattern. In the channel with a large gap, the central jet of fluid is much wider and

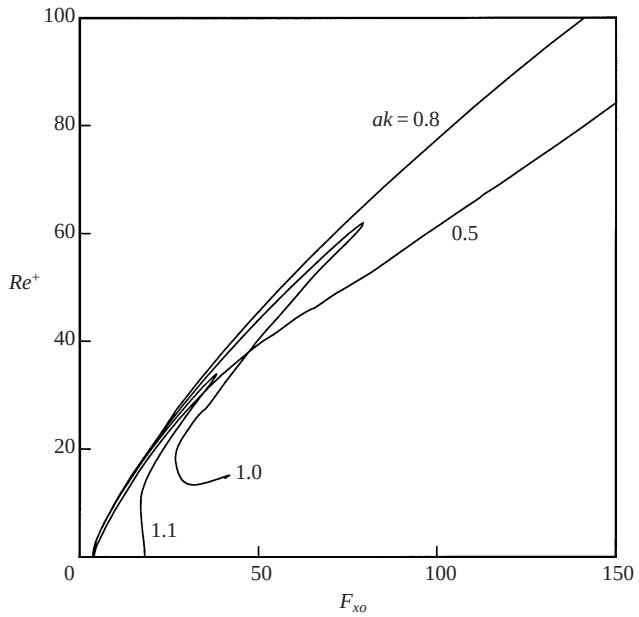

FIGURE 8. Bifurcation diagram showing degree of asymmetry Re^+ as a function of forcing level F_{xo}.

experiences little deceleration, hence maintaining its stability over a larger range of forcing. In comparing the flow rate dependence for the three channels with varying gap size, we observe that the curvature is greatest for the smallest gap and decreases montonically for increasing h/a. This illustrates the increasing importance of the inertial effects due to the strong acceleration/deceleration present in channels with severe constrictions. Recall that Poiseuille flow in an unconstricted channel yields a linear dependence on F_{xo} for all Reynolds numbers.

We now turn our attention to channels with different wall slopes, holding the gap size constant at $h/a = 0.1$. Figure 7(c,d) shows the flow rate for channels with maximum slopes $ak = 0.5$ and $a/k = 2$ respectively. For the case $ak = 0.5$, we observe the first symmetry-breaking bifurcation at approximately the same forcing level as for the $ak = 1$ case. With the smaller wall slope however, the asymmetric solution branch extends to higher Reynolds numbers with no turning points. If we examine the streamline pattern in figure 5(d), we see that the jet of fluid along the wall possesses a large amount of y-momentum, and it must be deflected from this upward course and turn to exit through the constriction. At higher flow rates, the jet acquires too much momentum and is unable to make the turn at the exit of the channel; hence the turning point on the bifurcation diagram. In contrast, for the smaller wall slope $ak = 0.5$, the fluid has less momentum in the y-direction (figure 7c) and can more easily make the change in direction required to flow out of the constriction. Thus the asymmetric branch shows no turning points over the entire forcing range. For the case of a larger wall slope, shown in figure 7(d), we find only a single symmetric solution with no bifurcations or turning points. It is possible however that additional solutions may exist in this forcing range arising from turning points at higher Reynolds numbers or from distinct solution branches originating at infinity.

Given our inability to discover additional solutions for the case of large wall slope $ak = 2$, we turn to a bifurcation diagram, figure 8, and examine the change in behaviour for a number of different wall slopes. As noted above, the Re^+ plot shows

the degree of asymmetry in the flow, hence all symmetric solutions, including that for $ak = 2$ lie on the horizontal axis. We begin with the curve for $ak = 1$, shown previously in figure 6(b). This shows two turning points near $F_{xo} = 26$ and $F_{xo} = 80$. The short branch extending from the turning point at $F_{xo} = 26$ represents solution 5(b) and ends at another turning point near $F_{xo} = 42$. Our arc-length continuation algorithm failed to locate additional solutions past this turning point.

Given this behaviour for $ak = 1$, we considered channels with slightly higher and lower wall slopes with $ak = 1.1$ and $ak = 0.8$ respectively. For $ak = 1.1$, all turning points and the entire solution curve have migrated toward lower forcing and smaller Re^+. When we attempted parameter continuation to extend the solution space to higher ak, the continuation algorithm failed for all asymmetric solution branches. The flow structure appears to be very sensitive to changes in wall slope for $ak > 1$. For $ak = 0.8$, we see a different behaviour with no turning points up to a Reynolds number of 200. Over this range, we found only the single asymmetric branch analogous to figure 5(d). Again, it is quite likely that additional turning points will be encountered at higher Re_o or F_{xo}, and the branches may lead back to additional solutions at more moderate F_{xo}, but we did not discover such solutions in our studies. The final curve in figure 8 for the case $ak = 0.5$ shows no turning points and a trend toward a smaller degree of asymmetry.

The bifurcation behaviour illustrated in figure 8 is quite complicated, and it is difficult to completely characterize the changes in bifurcation structure as a function of channel geometry. It is clear from this figure however, that the bifurcation curves do not show a simple monotonic evolution as one moves from slopes of $ak = 0.5$ to $ak = 1.1$. Owing to this behaviour, it would be impossible to predict the bifurcation structure for high wall slopes based on extrapolations from small slope geometries. In addition, the large wall slopes introduce significant qualitative differences in these flows compared to the channel flows studied by Sobey & Drazin and Goodwin & Schowalter.

While the bifurcation diagram for Re^+ shows a complicated solution structure which we have not fully resolved, the most important conclusions for our present study carry over from the results for our initial geometry $ak = 1, a/h = 0.1$. At low forcing levels a single stable symmetric solution branch exists. At higher forcing levels, multiple solutions may exist with stable solutions taking an asymmetric form. If real media have explicit geometric asymmetry, one may conjecture that such geometries would be further inclined toward asymmetric solutions. In all cases, the bulk flow rate is a nonlinear function of the forcing level with the degree of nonlinearity increasing as the ratio of pore size to constriction size increases. Differences in flow rate among multiple solutions at a given forcing level remain small in all cases examined here.

3.2. *Cylinder array*

In this section we present results for the cylinder array model. This model has many features similar to the constricted channel, but allows one to examine the effects of forcing in arbitrary directions. Since fluid can flow out of the domain in both the x- and y-directions, the mean velocity is a vector quantity whose dimensionless form is the vector Reynolds number $\boldsymbol{Re}_o$ with components Re_{xo} and Re_{yo}.

Inertial flow in cylinder arrays has been studied recently by Koch & Ladd (1997). A combination of theoretical analyses and numerical simulations was employed to study the impact of inertial effects on the drag force on the cylinder. A first measure of the sensitivity of the flow resistance to nonlinear inertial effects may be obtained

by considering the asymptotic results for small but finite Reynolds numbers. Koch & Ladd show that the low Reynolds number asymptotic result for forcing level versus Reynolds number may be written (in their notation)

$$\frac{F}{\mu U} = Re\,(k_0 + k_2 Re^2), \tag{3.2}$$

where the coefficient k_2 measures the initial sensitivity to inertial effects. Using k_2 as a guide (see Koch & Ladd, figure 3), we may organize the results for cylinder arrays into three regimes depending on the solid volume fraction. In the low volume fraction regime $\phi \leqslant 0.05$, k_2 is a strong function of volume fraction and takes on large values $\sim \phi^{-1}$ as ϕ approaches zero. In the moderate volume fraction regime $0.05 \leqslant \phi \leqslant 0.40$, k_2 is relatively small and insensitive to volume fraction. Finally, for high volume fractions, $\phi > 0.40$, the flow resistance begins to be dominated by lubrication flow in the constriction, and k_2 is again a strong function of volume fraction. In the limit as ϕ approaches the maximum packing fraction, Koch & Ladd show that k_2 approaches infinity as $h^{-3/2}$. Koch & Ladd have given a detailed analysis of the flow through cylinder arrays in the low and moderate volume fraction regimes. They develop asymptotic theories and conduct a wide range of numerical simulations to investigate changes in the flow structure as a function of Reynolds number. They discuss these results with application to the anisotropy of the permeability, and transition to time-oscillatory and chaotically varying flows.

In the present paper, our objective is to use the cylinder array model to study strong oscillatory forcing perpendicular to the direction of the mean pressure gradient. We are interested in porous media with relatively high volume fractions, and this regime is beyond the range covered by the numerical simulations of Koch & Ladd. In this effort, we seek to document the onset of flow bifurcations and to study the nonlinear flow phenomena relevant for these systems. In our numerical study, we cover a wide range of Reynolds numbers up to $Re_o = 90$. While this is beyond the formal range of the low-Re lubrication theory of Koch & Ladd, we find that the lubrication results provide good estimates in many cases. In other cases, we shall see the limitations of the simple lubrication theory and identify new phenomena associated with the asymmetric flow patterns at finite Re.

We begin our study by examining flows with horizontal forcing parallel to the x-direction. We set the parameter $h/r = 0.0329$ so that the ratio of the gap size to channel length is the same as that for the constricted channel with $ak = 1$ and $h/a = 0.1$. With this choice the solid volume fraction ϕ is equal to 0.736. The streamline patterns for a range of forcing levels are presented in figure 9. The flow patterns are very similar to those observed for constricted channels: a symmetric flow is observed for low forcing levels and asymmetric solutions are observed for higher forcing levels. The symmetric flow is characterized by a jet of fluid that passes through the centre of the cylinder array and the absence of flow in the y-direction. In contrast, the asymmetric solution induces a transverse flow through the bottom of the domain with dimensionless flow rate $Re_{yo} = -4.40$. The bending of the fluid jet produces a stagnation point on the downstream cylinder wall, and the sharp turn at the stagnation point generates momentum in the y-direction which carries a portion of the fluid out through the bottom of the domain. We note that the mirror image of this flow may also arise, in which the fluid jet bends in the opposite direction, and the net flow is out through the top of the domain. In either case, the direction of the mean velocity is diverted from the direction of the applied pressure gradient, and the effective permeability must be represented as an anisotropic tensor.

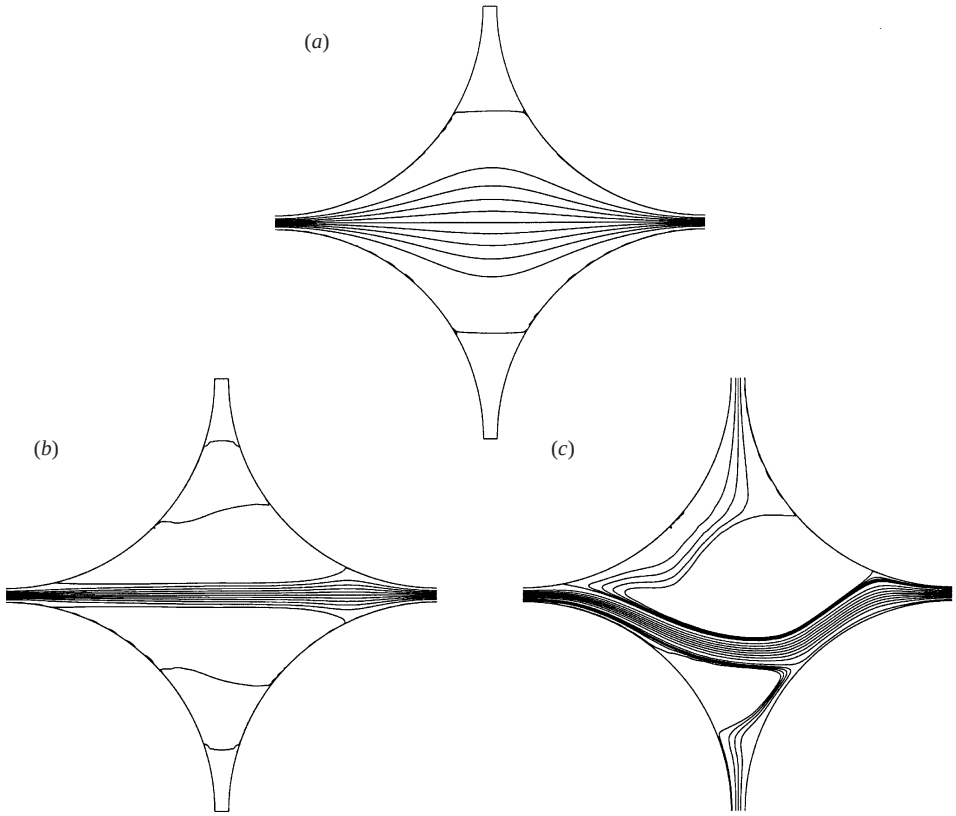

FIGURE 9. Streamline patterns for cylinder arrays at various axial forcing levels and zero cross-forcing $F_{yo} = 0$. (*a*) $F_{xo} = 0.25$, $Re_{xo} = 0.560$, $Re_{yo} = 0$; (*b*) $F_{xo} = 35$, $Re_{xo} = 54.9$, $Re_{yo} = 0$; (*c*) $F_{xo} = 35$, $Re_{xo} = 53.0$, $Re_{yo} = -4.40$.

To continue the characterization of the steady solution behaviour, the flow rate for the different solution branches is shown in figure 10(*a*). These results are similar to those shown earlier for the constricted channel. At low forcing, a unique symmetric solution exists; however, as the forcing is increased, a bifurcation point is encountered and the symmetric solution loses stability to an asymmetric solution. The two solution branches continue to exist as F_{xo} is increased and no turning points are observed. To compare the numerical results with the predictions of lubrications analysis, we employ Koch & Ladd's equation (11) which gives the pressure drop as a function of *Re*. Casting this result into the notation of the present paper, we have†

$$F_o = Re_o(m_0 + m_2 Re_o^2), \tag{3.3}$$

where

$$m_0 = \frac{9\pi}{8}\left(\frac{h}{L}\right)^{1/2}, \quad m_2 = \frac{624\pi}{13475}\left(\frac{r}{L}\right)^2\left(\frac{h}{L}\right)^{3/2}. \tag{3.4}$$

† In calculating the total force, we multiply Δp by the total height L of the unit cell, whereas Koch & Ladd simply multiplied by $2r$. Their result is correct to leading order but leads to an additional error of order h/L even at $Re = 0$.

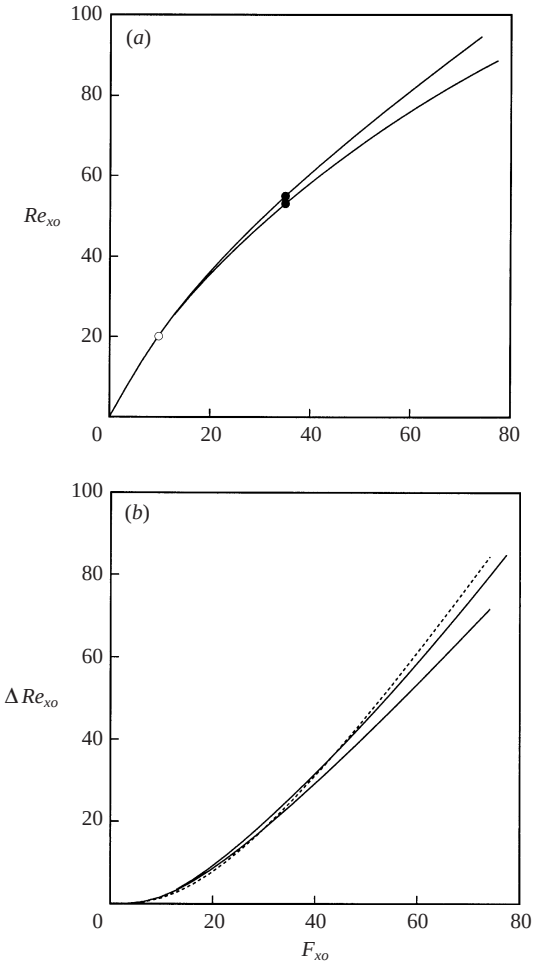

FIGURE 10. (*a*) Flow rate for cylinder array with $F_{yo} = 0$. The open circle indicates the bifurcation point and the solid circles indicate the locations of the streamline patterns shown in figure 9(*b*) and 9(*c*). (*b*) Differential change in flow rate compared to the Darcy regime; dashed line represents lubrication prediction from equation (3.3).

To focus on the nonlinear inertial effects, we compute the difference between the Darcy flow F_{xo}/m_0 and the actual flow rate and define

$$\Delta Re_{xo} = \frac{F_{xo}}{m_0} - Re_{xo}. \tag{3.5}$$

The value of ΔRe_{xo} predicted by the lubrication result (3.3) is compared to the numerical solutions in figure 10(*b*). The lubrication theory does an excellent job in predicting the overall flow rate over a wide range of forcing levels and Reynolds numbers. Note that the lubrication theory cannot distinguish between the symmetric and asymmetric solutions in the broad open regions of the channel.

With the flow behaviour for axial forcing with $F_{yo} = 0$ documented above, we now examine the permeability of the cylinder arrays with applied forcing in an arbitrary direction. For Stokes flow, the permeability is isotropic, which implies that the direction of the mean velocity is always parallel to the direction of forcing, and

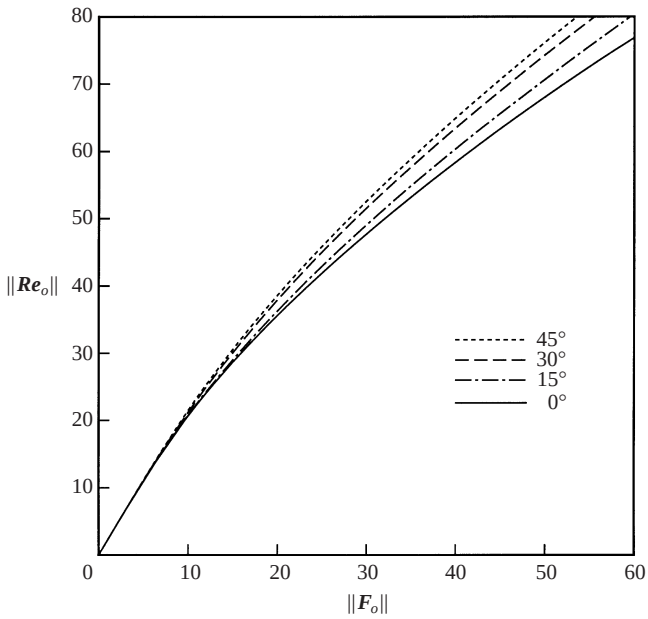

FIGURE 11. Magnitude of the Reynolds number vs. magnitude of forcing for different angles of forcing.

the magnitude of the flow rate is independent of the direction of forcing. For inertial flows this is not the case, as shown in figures 11 and 12. In these figures, the magnitude and direction of the mean flow is shown as a function of the magnitude of the forcing level. In figure 11, for low forcing levels all of the curves collapse to the same line, due to the decreased importance of inertial effects. As the forcing level increases, the anisotropic nature becomes more apparent, with pressure gradients closer to 45° resulting in larger flow rates/Reynolds numbers. For flow through the narrow gaps in this geometry, the inertial forces act to increase the flow resistance as the flow rate increases. For forcing at small angles, the total fluid volume must travel through a single gap, with stagnant fluid regions in the vertical gaps. As the forcing angle increases toward 45°, the flow is split between two gaps on either side of the cylinder, and the inertial flow resistance is reduced. Figure 12 shows that the direction of the mean flow rate tends to move closer to 45° compared to the direction of the forcing level, because this angle represents the line of minimum resistance.

A quantitative prediction based on the physical arguments above follows immediately from lubrication analysis. The lubrication prediction of equation (3.3) may be applied to each component of the forcing vector $\boldsymbol{F}_o$, and the results employed to predict the angle of the mean flow field. This is essentially the procedure used by Koch & Ladd to arrive at their equation (15) except that their result employs additional algebraic approximations valid only for small Re. We find a better prediction by using equation (3.3) directly and numerically solving for the resulting angle. The lubrication predictions for angle of mean flow are shown in figure 12. Here we see that the lubrication theory is not as successful as in the previous case. For a forcing angle of 0°, the lubrication theory predicts a flow direction oriented at 0° while the numerical solutions show a departure from the direction of mean forcing of up to 8°. This departure is associated with the asymmetric flow patterns (for $F_{xo} \geqslant 10$) which induce a transverse flow in the y-direction even for purely axial forcing in

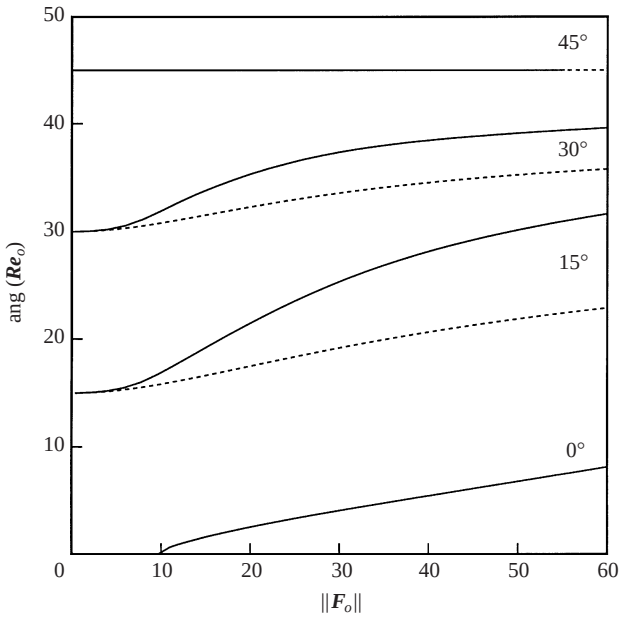

FIGURE 12. Angle of the flow direction vs. magnitude of forcing for different angles of forcing. Dashed lines give prediction of lubrication theory based on equation (3.3).

the x-direction. The numerical curves for forcing angles of 15° and 30° show a similar divergence compared with the lubrication prediction. For the final case with angle 45°, the sole solution branch yields a symmetric flow and both lubrication and numerical solutions give a flow angle of exactly 45°. We conclude that the anisotropy of the porous medium is associated with two distinct flow phenomena. The first, drag reduction associated with reduced inertial forces by splitting the flow into two streams, is captured well by lubrication theory. The second, transverse flow induced by asymmetric flow patterns, requires a detailed knowledge of the flow field in the large open areas of the channel.

Having characterized the flow behaviour of a cylinder array with a relatively high solid fraction ($\phi = 0.736$), we now consider the effect of changes in solid fraction ϕ on the permeability. The dependence of the flow rate on the solid fraction for two different forcing angles (0°, 45°) is shown in figure 13. For high solid fractions, we recall that the permeability is greater for a forcing angle of 45°. However, for low solid fractions, we observe greater flow rates for a forcing angle of 0°. Koch & Ladd have noted that the main component of the flow resistance for arrays with low volume fraction is from drag. This drag force is reduced when the forcing is at 0° because the cylinders are closer together, and the wake from one cylinder shields the next cylinder downstream, i.e. the familiar *drafting* effect. For cylinder arrays at dilute to moderate volume fractions (up to $\phi = 40°$), these authors give a detailed discussion of the changes in flow character as a function of volume fraction and Reynolds number. They include additional discussion on the transition to unsteady flows under steady forcing conditions and the resulting effects on flow angle. Based on these effects, for high Reynolds number flows, Koch & Ladd conclude that it is very difficult to drive a flow through a square cylinder array at any angle other than parallel to an array axis. Given the results of our study, we would qualify that conclusion and state that it applies for a range of low to moderate volume fractions for which drafting effects

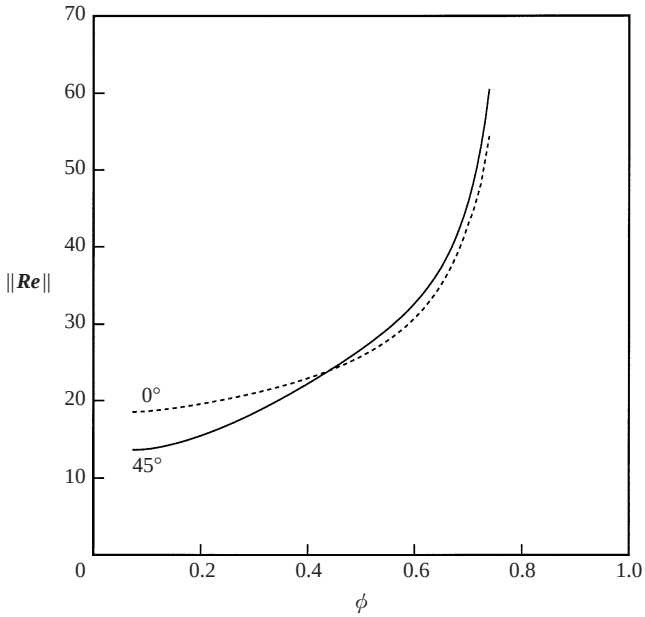

FIGURE 13. Magnitude of $\boldsymbol{Re}_o$ as a function of solid volume fraction for $\|\boldsymbol{F}_o\| = 35$.

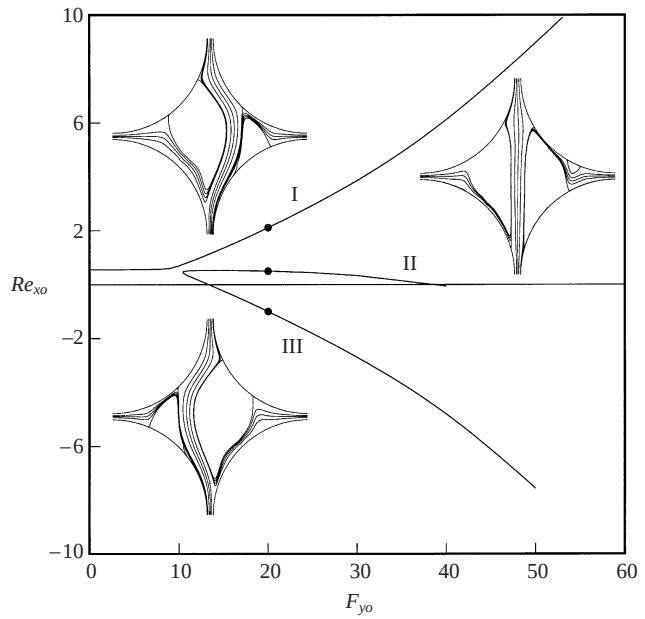

FIGURE 14. Bifurcation diagram for cylinder array with weak axial forcing $F_{xo} = 0.25$ showing the effect of increasing cross-flow forcing.

are important. As one approaches the high volume fraction regime dominated by the lubrication flow in constrictions, drafting effects becomes less important, and other considerations will dictate the direction of mean flow.

Next, we consider a different approach in examining the effect of the forcing direction on the flow rate. We hold the forcing in the x-direction constant at a low

level, $F_{xo} = 0.25$, and consider changes in the x velocity subject to variation in the y forcing level F_{yo}. The flow rate/bifurcation diagram together with representative streamline plots is shown in figure 14. For small transverse forcing F_{yo}, a single solution exists in which the flow rate Re_{xo} is relatively unaffected by the small amount of forcing in the y-direction. As we increase F_{yo}, the solution structure becomes more complicated and multiple solutions are observed. Focusing on branch I, we observe that Re_{xo} increases dramatically with increasing F_{yo}. The jet of fluid passing through the centre is bent and tends to steer the fluid out of the domain in the positive x-direction. Turning our attention to branch II, we observe that Re_{xo} is less affected by F_{yo}, because the jet of fluid bends to a lesser degree. Following branch II past the turning point reveals branch III, where the trend is opposite to branch I. The bend in the fluid jet now opposes the forcing in the x-direction, decreasing the flow rate, and eventually reversing the sense of flow in the x-direction. Unsteady calculations with constant forcing indicate that both branch I and branch III are stable and that branch II is unstable. Our objective in this figure is to illustrate the effect of strong transverse forcing on the mean flow subject to a weak pressure gradient. As we have seen in branches I and III, the transverse forcing may have a strong effect on the x flow rate; however, this effect may act to increase or to decrease the flow rate with equal likelihood. This behaviour will have significant implications for acoustic stimulation of flow in porous media, as discussed in Part 2.

Given our interest in acoustic stimulation, it is natural to view figure 14 as the result of strong lateral forcing and its effect on a weak mean flow. It should be noted however that the bifurcation pattern seen in this figure is well known in the literature on nonlinear systems. In the limit as the axial forcing F_{xo} approaches zero, the bifurcation diagram yields a classic pitchfork bifurcation with Re_{xo} acting as a control parameter measuring flow asymmetry. The forcing F_{xo} acts as a small perturbation yielding the perturbed pitchfork bifurcation seen in figure 14. These bifurcation diagrams have significance in many applications as they characterize the effect of imperfections in the system geometry on operation. Fearn *et al.* (1990) show an example of this behaviour in their computations and experiments for asymmetric flows downstream of a channel expansion.

4. Conclusions

We have analysed the steady flow behaviour for two distinct geometric models of porous media. For flow through constricted channels, we have shown that inertial effects lead to multiple solutions over a broad spectrum of geometric parameters. A unique symmetric solution exists at low forcing levels; however, this solution loses stability to an asymmetric solution as the forcing is increased. The asymmetric solution has a higher flow resistance than the symmetric solution.

A cylinder array model showed similar behaviour to the constricted channels with respect to multiple steady-state solutions. The cylinder arrays allow consideration of pressure gradients in arbitrary directions and exhibit anisotropic behaviour for sufficiently high Reynolds numbers. The direction of forcing leading to the maximum flow rate is strongly dependent on the solid volume fraction.

The nonlinear flow phenomena which we have studied in this paper have significant implications for acoustic stimulation of single-phase flow in porous media. For the linear regime where the flow rate is proportional to the pressure gradient, the addition of an oscillatory force with zero mean can produce no net increase in the average flow rate. Any enhancement of the fluid transport rate depends on nonlinear

phenomena. In this paper, we have seen three distinct manifestations of nonlinear phenomena which might be exploited by an oscillatory forcing function. The first is the nonlinear dependence of flow rate on driving force. This nonlinearity may lead to a non-zero mean flow driven by a purely oscillatory driving force. A detailed discussion will be presented in Part 2. The second phenomenon is the existence of multiple solutions with different flow rates at the same forcing level. When a porous medium is subjected to an oscillatory driving force, the instantaneous driving force sweeps back and forth across the axis of the diagrams relating flow rate and pressure gradient. The solution branch which is selected may depend not only on the instantaneous forcing level, but also on the forcing level at previous instants. This leads to the possibility of hysteresis loops with a positive mean flow rate arising from the different solution branches selected on the forward and reverse portions of the driving cycle. The third phenomenon is associated with the anisotropy arising in the cylinder arrays at finite Reynolds number. We have seen that the mean flow in the x-direction may be significantly affected by a strong transverse pressure gradient with equal likelihood of enhancement or retardation. A transverse oscillatory driving force might excite a favourable (or unfavourable) axial flow in both portions of its cycle, thereby increasing (or decreasing) the mean flow rate by selection of the appropriate solution branch. This hysteresis loop may also be initiated by a purely transverse pressure force with no driving force in the direction of the mean flow.

While the nonlinear phenomena identified in this paper might lead to enhanced transport in the presence of oscillatory driving forces, the final disposition of the flow will depend on the influence of the unsteady inertial terms in the time-dependent Navier–Stokes equations. The analysis of these terms and their effect on predictions based on steady flow phenomena is taken up in Part 2.

This work was supported by a grant from the National Science Foundation. D. R. Graham acknowledges the support of a Computational Science and Engineering Fellowship from the University of Illinois. Computational resources were provided by IBM through the Shared University Resource Program at the University of Illinois, and by the National Center for Supercomputing Applications.

REFERENCES

Beresnev, I. A. & Johnson, P. A. 1994 Elastic-wave stimulation of oil production: A review of methods and results. *Geophysics* **59**, 1000–1017.

Deiber, J. A. & Schowalter, W. R. 1979 Flow through tubes with sinusoidal axial variations in diamter. *AIChE J.* **25**, 638–644.

Demmel, J. W., Eisenstat, S. C., Gilbert, J. R., Li, X. S. & Liu, J. W. H. 1995 A supernodal approach to sparse partial pivoting. *Tech. Rep.* University of California, Berkeley.

Dimitrakopoulos, P. & Higdon, J. J. L. 1997 Displacement of fluid droplets from solid surfaces in low-*Re* shear flows. *J. Fluid Mech.* **336**, 351–378.

Dimitrakopoulos, P. & Higdon, J. J. L. 1998 On the displacement of three dimensional fluid droplets from solid surfaces in low Reynolds number shear flows. *J. Fluid Mech.* **377**, 189–222.

Drake, T. & Beresnev, I. A. 1999 Acoustic tool enhances oil production. *Am. Oil & Gas Reporter* Sept. 1999.

Edwards, D. A., Shapiro, M., Bar-Yoseph, P. & Shapira, M. 1990 The influence of Reynolds number upon the apparent permeability of spatially periodic arrays of cylinders. *Phys. Fluids* A **2**, 45–55.

Fearn, R. M., Mullin, T. & Cliffe, K. A. 1990 Nonlinear phenomena in a symmetric sudden expansion. *J. Fluid Mech.* **211**, 595–608.

FRAENKEL, L. E. 1962 Laminar flow in symmetrical channels with slightly curved walls I. On the Jeffrey-Hamel solutions for flow between plane walls. *Proc. R. Soc. Lond.* A **267**, 119–138.

FRAENKEL, L. E. 1963 Laminar flow in symmetrical channels with slightly curved walls II. An asymptotic series for the stream function. *Proc. R. Soc. Lond.* A **272**, 119–138.

GOODWIN, R. T. & SCHOWALTER, W. R. 1996 Interactions of two jets in a channel: solution multiplicity and linear stability. *J. Fluid Mech.* **313**, 55–82.

GRAHAM, D. R. & HIGDON, J. J. L. 2000*a* Oscillatory flow of droplets in capillary tubes. Part 1. Straight tubes. *J. Fluid Mech.* **425**, 31–53.

GRAHAM, D. R. & HIGDON, J. J. L. 2000*b* Oscillatory flow of droplets in capillary tubes. Part 2. Constricted tubes. *J. Fluid Mech.* **425**, 55–77.

GRAHAM, D. R. & HIGDON, J. J. L. 2002 Oscillatory forcing of flow through porous media. Part 2. Unsteady flow. *J. Fluid Mech.* **465**, 237–260.

HASIMOTO, H. 1959 On the periodic fundamental solutions of the Stokes equations and their applications to viscous flow past a cubic array of cylinders. *J. Fluid Mech.* **5**, 317–328.

HEMMAT, M. & BORHAN, A. 1995 Creeping flow through sinusoidally constricted capillaries. *Phys. Fluids* **7**, 2111–2121.

HUYAKORN, P. S., TAYLOR, C., LEE, R. L. & GRESHO, P. M. 1978 A comparison of various mixed-interpolation finite element in the velocity-pressure formulation of the Navier–Stokes equations. *Comput. Fluids* **6**, 25–35.

KELLER, H. B. 1977 Numerical solution of bifurcation and nonlinear eigenvalue problems. In *Applications of Bifurcation Theory* (ed. P. H. Rabinovich), pp. 359–384. Academic.

KOCH, D. L. & LADD, A. J. C. 1997 Moderate Reynolds number flows through periodic and random arrays of aligned cylinders. *J. Fluid Mech.* **349**, 31–66.

LARSON, R. E. & HIGDON, J. J. L. 1987 Microscopic flow near the surface of two-dimensional porous media. Part 2. Transverse flow. *J. Fluid Mech.* **178**, 119–136.

POZRIKIDIS, C. 1987 Creeping flow in two-dimensional channels. *J. Fluid Mech.* **180**, 495–514.

RALPH, M. E. 1987 Steady flow structures and pressure drops in wavy-walled tubes. *Trans ASME*: *J. Fluids Engng* **109**, 255–261.

SANGANI, A. S. & ACRIVOS, A. 1982 Slow flow past periodic arrays of cylinders with application to heat transfer. *Intl J. Multiphase Flow* **8**, 193–206.

SOBEY, I. J. & DRAZIN, P. G. 1986 Bifurcations of two-dimensional channel flows. *J. Fluid Mech.* **171**, 263–287.

THOMPSON, J. F., WARSI, Z. U. A. & MASTIN, C. W. 1985 *Numerical Grid Generation*. Elsevier.